Observation of Spin-Momentum-Layer Locking in a Centrosymmetric Crystal

Ke Zhang,[1,*] Shixuan Zhao,[2,*] Zhanyang Hao,[2,*] Shiv Kumar,[3] Eike. F. Schwier,[3,6,7] Yingjie Zhang,[2] Hongyi Sun,[2] Yuan Wang,[2] Yujie Hao,[2] Xiaoming Ma,[2] Cai Liu,[2] Le Wang,[2] Xiaoxiao Wang,[3] Koji Miyamoto,[3] Taichi Okuda,[3] Chang Liu,[2] Jiawei Mei,[2] Kenya Shimada,[3,†] Chaoyu Chen,[2,‡] and Qihang Liu[2,4,5,§]

[1]*Department of Physical Science, Graduate School of Science, Hiroshima University, Hiroshima 739-0046, Japan*
[2]*Shenzhen Institute for Quantum Science and Technology and Department of Physics,*
Southern University of Science and Technology, Shenzhen 518055, China
[3]*Hiroshima Synchrotron Radiation Center, Hiroshima University, Hiroshima 739-0046, Japan*
[4]*Guangdong Provincial Key Laboratory for Computational Science and Material Design,*
Southern University of Science and Technology, Shenzhen 518055, China
[5]*Shenzhen Key Laboratory of Advanced Quantum Functional Materials and Devices,*
Southern University of Science and Technology, Shenzhen 518055, China
[6]*Experimentelle Physik VII, Universität Würzburg, Am Hubland, D-97074 Würzburg, Germany*
[7]*Würzburg-Dresden Cluster of Excellence ct.qmat, Germany*

The spin polarization in nonmagnetic materials is conventionally attributed to the outcome of spin-orbit coupling when the global inversion symmetry is broken. The recently discovered hidden spin polarization indicates that a specific atomic site asymmetry could also induce measurable spin polarization, leading to a paradigm shift in research on centrosymmetric crystals for potential spintronic applications. Here, combining spin- and angle-resolved photoemission spectroscopy and theoretical calculations, we report distinct spin-momentum-layer locking phenomena in a centrosymmetric, layered material, BiOI. The measured spin is highly polarized along the Brillouin zone boundary, while the same effect almost vanishes around the zone center due to its nonsymmorphic crystal structure. Our work demonstrates the existence of momentum-dependent hidden spin polarization and uncovers the microscopic mechanism of spin, momentum, and layer locking to each other, thus shedding light on the design metrics for future spintronic materials.

Introduction.—Strategies for generating and controlling highly spin-polarized electronic states in nonmagnetic solids have been explored extensively, taking a crucial step towards the realization of novel spintronic devices [1–6]. It is generally believed that such processes require breaking the space inversion symmetry. This is because a combination of both time-reversal and inversion symmetries inevitably yields spin-degenerate energy levels; further, a spin splitting induced by the spin-orbit coupling (SOC) Hamiltonian [7] is typically classified as the Dresselhaus type [8] or Rashba type [9], according to the specific form of inversion symmetry breaking. Recently published studies have indicated that local symmetry breaking (e.g., polar field) within a part of a unit cell (termed as a "sector") can intrinsically lead to a form of "hidden spin polarization" (HSP) in most centrosymmetric crystals [10,11]. The global inversion symmetry ensures the existence of an inversion counterpart for a given sector, manifesting exactly opposite HSP and thus leading to spin-degenerate energy bands in the momentum space. However, in the real space, there are indeed spin polarizations localized on both sectors [11–14]. Instead of the arbitrary choices of sector partition in a centrosymmetric

system (the wave function basis according to different choices of sectors can be connected by a unitary transformation), when an individual part is predominantly detected by the probe, the partition of the whole unit cell into sectors is naturally selected. As a result, the choice for the sector could be a van der Waals layer (e.g., in bulk WSe_2 [15]), a sublattice [16], or even an atomic layer (e.g., Se in the $PtSe_2$ monolayer [17]), and the corresponding HSP effect can be measured by spin- and angle-resolved photoemission spectroscopy (spin-ARPES) [15,17–24] as well as by polarized optical measurements [25–27]. Hence, the experimental evidence of HSP have been reported based on various layered materials such as bulk and monolayer transition metal dichalcogenides [15,17,18,22], $BaNiS_2$ [20], $LaO_{0.55}F_{0.45}BiS_2$ [23], and Bi2212 cuprate superconductor [24].

Exploring different quantum materials with strong HSP effects could considerably expand the choice of materials for nonmagnetic spintronic devices. However, while the local symmetry breaking in the real space is the essential characteristic of the HSP, its underlying physics, involving the microscopic mechanism of the way the spin, momentum,
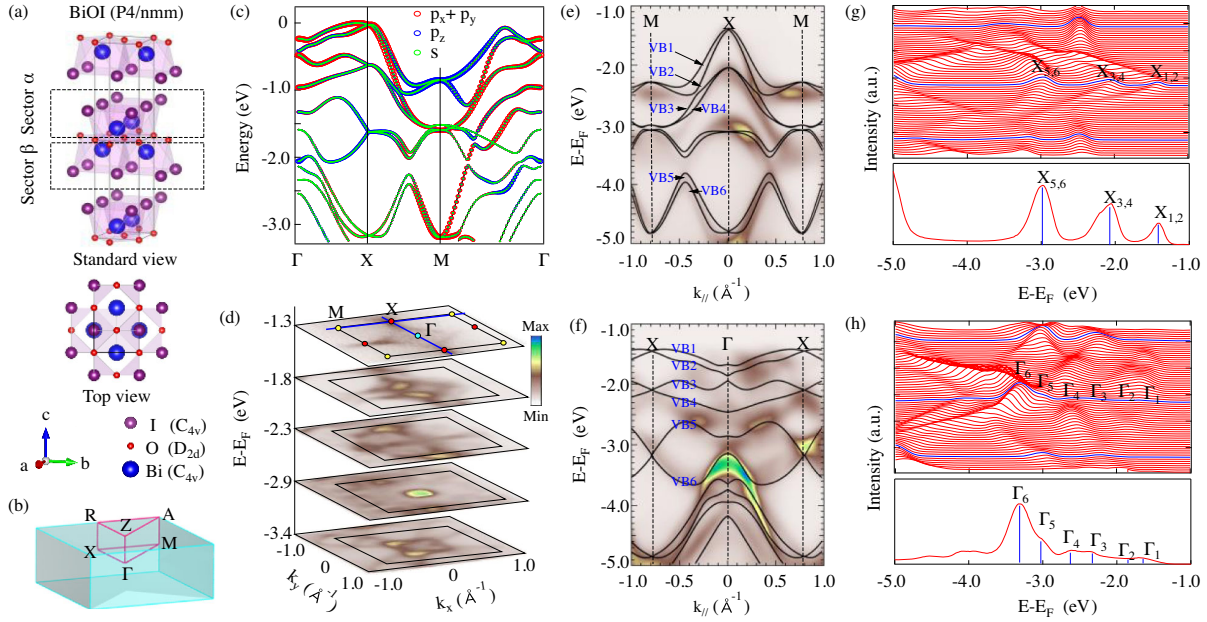
FIG. 1. (a) The crystal structure of BiOI. The unit cell consists of two BiI layers as inversion partners, labeled as a sector α and β. (b) The bulk Brillouin zone. (c) DFT-calculated bulk band dispersion with orbital projection. (d) ARPES-measured CECs of the valence bands at different energies. (e),(f) ARPES-measured spectra along the $X - M$, and $\Gamma - X$ high symmetry lines, overlaid by DFT calculated dispersions (solid black lines). (g),(h) EDCs corresponding to the spectra shown in (e) and (f), respectively. The lower parts are the EDCs at the X and Γ points, respectively, from which one can resolve the spectral peaks corresponding to the top six valence bands.

and sector lock to each other, remains elusive. Recent theoretical works predicted that the magnitude of the HSP effect is distinct around the Brillouin zone (BZ) center and the BZ boundary [16]. Here, by using systematic spin-ARPES measurements, we have investigated the electronic structure and particularly, the spin polarization of a single crystal BiOI with nonsymmorphic symmetry. We have observed up to 80% net spin polarization along the BZ boundary ($X - M$) but almost zero net spin polarization around Γ, indicating a unique momentum dependence of the HSP effect. Our tight-binding (TB) model, as well as density functional theory (DFT) calculations, revealed that in contrast to the Γ point, the nonsymmorphic symmetry minimizes the spin compensation between adjacent sectors at the BZ boundary, thus successfully retaining the local spin polarization of each sector. Our findings reveal the delicate interplay between spin-momentum-sector locking and symmetry protection in HSP systems, thus shedding light on the possibility of all-electrical manipulation.

Electronic structure.—BiOI is an ideal semiconductor, with the Fermi level being easily tunable by doping; therefore, it has been extensively used in the visible light photocatalysis studies [28]. BiOI has a tetragonal crystal structure with a centrosymmetric space group $P4/nmm$ containing nonsymmorphic operations of a glide mirror $\{M_z|(\frac{1}{2},\frac{1}{2},0)\}$ and two screw axes $\{C_{2x}|(\frac{1}{2},0,0)\}$, $\{C_{2y}|(0,\frac{1}{2},0)\}$. The inversion center is located in the middle of two inequivalent O atoms (site point group D_{2d}), while the Bi and I atoms occupy the noncentrosymmetric polar sites with the site point

group C_{4v}. The polyhedrons coordinated by Bi and I atoms are intersected by the O plane. Hence, the quasi-2D unit cell is divided into two sectors α and β, respectively, as shown in Fig. 1(a). The global centrosymmetric structure creates opposite local polar fields along the c axis felt by each BiI layer, which is a prerequisite for the HSP effect [16].

The BZ and DFT-calculated electronic structures of BiOI with SOC are shown in Figs. 1(b) and 1(c) [29]. The valence band maximum (VBM) is close to the X point. It is noticeable that at the points X and M, the glide reflection symmetry $\{M_z|(\frac{1}{2},\frac{1}{2},0)\}$ anticommutes with the inversion operator, leading to an extra twofold degeneracy between two pairs of Kramer's degeneracy, i.e., fourfold degeneracy including the spin. Such a fourfold degeneracy is maintained along the entire $X - M$ line in the absence of SOC [29]. Thus, the band splitting along the $X - M$ line shown in Fig. 1(c) is caused by SOC solely. In analogy to the conventional Rashba-Dresselhaus effect, such a splitting is composed of two sets of spin splitting bands originating from the sectors α and β [16]. In comparison, the splitting along the $\Gamma - X$ line is contributed by both the orbital repulsions and the SOC effect, and is thus larger than that along the $X - M$ line. The orbital projection analysis shows that in the vicinity of the points Γ and X, the top two valence bands (designated as VB1 and VB2) are mainly composed of the $p_x + p_y$ and s orbitals, while VB3-VB6 are dominated by the p_z and s orbitals.

The high quality BiOI samples in this study has been confirmed by core-level photoemission spectroscopy and
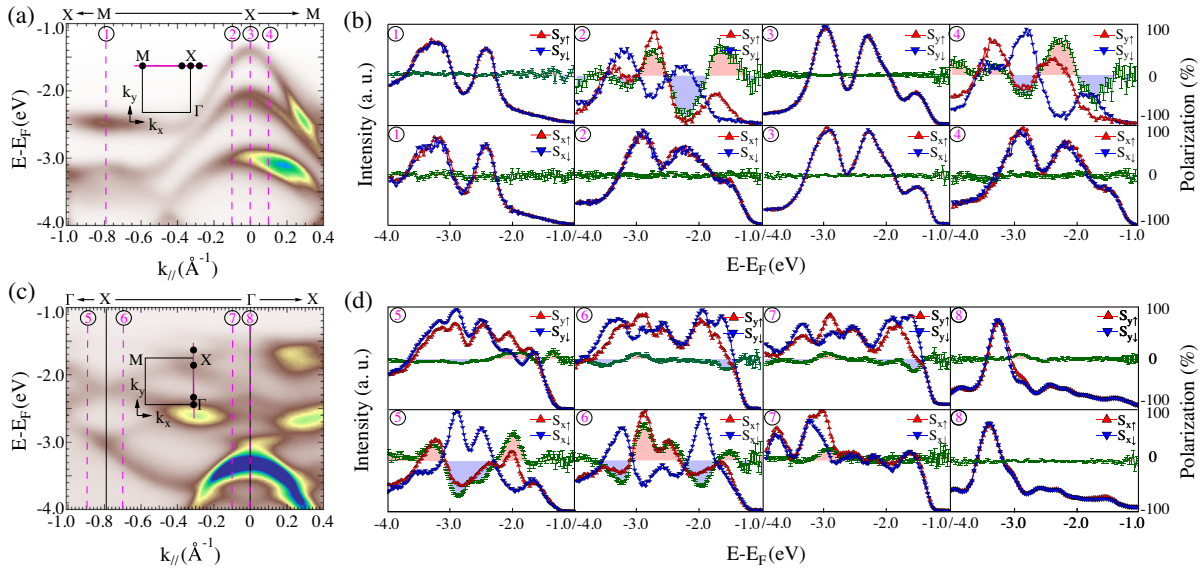
FIG. 2. (a),(c) Band dispersion along the $M - X$ and $\Gamma - X$ directions, respectively. The inset shows the BZ, with black dots indicating the momentum positions where the spin-resolved EDCs are measured. (b),(d) Spin-resolved EDCs and spin polarizations. Each panel's number corresponds to the momentum point denoted by the pink dashed lines in (a),(c). The green curves present the spin polarizations with statistical error bars proportional to $1/\sqrt{N}$, where N is the photoemission intensity.

x-ray diffraction [29]. The electronic structures of BiOI obtained by both DFT calculation and ARPES measurement [29] consistently show a 2D behavior with a relatively flat dispersion along the c axis. The ARPES results measured at a photon energy of 65 eV are shown in Fig. 1(d) [constant energy contours (CECs)], Figs. 1(e) and 1(f) (band dispersions) and Figs. 1(g) and 1(h) [energy-distribution curves (EDCs)]. As evident from our systematic photon energy-dependent measurement [29], this photon energy covers the 6th bulk Γ point, and a squarelike CEC exists at -1.3 eV, with corners located at X points. As the energy decreases, the CEC features at the X point expand and eventually form contours surrounding the M point, merging with those centered at the Γ point. This holelike behavior is presented in the ARPES spectra along the $M - X - M$ line in Fig. 1(e). From the CECs and spectra results, we have found that the VBM is located around the bulk X point, ~ 1.4 eV below the experimental Fermi level.

By directly comparing the calculated bulk band structure with the ARPES data shown in Figs. 1(e) and 1(f), a good agreement is found, indicating that the surface effect that breaks the global inversion symmetry is relatively weak. The predicted fourfold degeneracy at the X and M points and the splitting twofold degenerate branches (VB1 to VB6) away from X and M are all supported by the ARPES measured dispersion. Furthermore, Figs. 1(g) and 1(h) show the EDCs measured along the $M - X - M$ and $X - \Gamma - M$ directions. At the X point, the degenerate peaks, i.e., $X_{1,2}$, $X_{3,4}$, and $X_{5,6}$ are unambiguously present, while at the Γ point, each of the degenerate peak splits into two individual peaks, i.e., Γ_1 to Γ_6. Consequently, three

pairs of Rashba-like hole-type valence bands are formed at the X and M points, with the band crossing points located around -1.4, -2.1, and -3.0 eV for the X point, respectively [Fig. 1(e)]. These results agree well with our calculation that only the time-reversal invariant momenta at the BZ boundary (e.g., the X point) demonstrate a fourfold degeneracy, while the Γ point does not exhibit such behavior, thus confirming the nonsymmorphic feature of the material. We next use spin-ARPES measurements to further demonstrate that the HSP effects for two high-symmetry points (X and M) are clearly distinguishable.

Hidden spin polarization.—Figure 2 presents the in-plane spin polarization of BiOI measured by spin ARPES using photon energies of 65 eV for panels (a),(b) and 30 eV for panels (c),(d). Moreover, the spin-polarized EDCs from the horizontal $X - M$ direction, vertical $\Gamma - X$ direction, and horizontal $\Gamma - X$ direction are measured comprehensively as displayed in Ref. [29]. The wide-ranging measurements involving different photon energies and geometries verified that the observed spin polarization and spin textures are essentially intrinsic. The representative spin EDCs for the three pairs of twofold degenerate bands VB1–VB6 are shown in Figs. 2(b) and 2(d), with the upper (lower) row showing the spin-resolved EDCs and the corresponding S_y (S_x) spin component. At three time-reversal invariant points M, X, and Γ (momentum points ①, ③ and ⑧), the spin-resolved EDCs overlap, indicating negligible spin polarization; this is consistent with the spin degeneracy originating from Kramer's pairs.

When the momenta moved away from the X point, we have observed significant spin polarization (up to 80%) along both k_x and k_y directions (momentum points ②, ④, ⑤

and ⑥ [37]). For momenta ⑤ and ⑥, nearly all the six VBs were resolved as the individual polarizations peaked with opposing polarization signs in each pair. This is because the band splitting along $\Gamma - X$ direction was more significant compared to the splitting along the $X - M$ direction [Figs. 1(c), 1(e), and 1(f)]. In sharp contrast, the spin polarization surrounding the Γ point was very weak (<30%) for momentum point ⑦ and [29], along both k_x and k_y directions. It is worth noting that, for all the spin-resolved EDCs shown in Figs. 2(b) and 2(d), the sums of each pair as spin-integrated EDCs coincide with EDCs measured by regular ARPES in the overall spectral shape [29], a proof of accuracy and self-consistency of our measurement.

Because of the short photoelectron escape depth, ~5 Å [38], for the photoelectron kinetic energies of 20–100 eV, and a large lattice constant $c = 9.12$ Å [39], the detected photoemission signal mainly arises from the topmost sector (α) of the cleaved BiOI single crystal, which is favorable to detect the spin polarization from a local sector. Compared with the previous measurements of HSP materials such as WSe_2 [15], $PtSe_2$ [17], $LaO_{0.55}F_{0.45}BiS_2$ [23], and Bi2212 [24], which focus on the spin-momentum locking around a single high-symmetry point, our work revealed the distinct polarization features surrounding different high-symmetry points, i.e., BZ center (Γ) and BZ boundary (X), and observed a sharp contrast between them. Such observations suggest that momentum-dependent spin polarization originates from the HSP rather than merely from the surface potential gradient; further, these observations suggest the key factors affecting the HSP effect, such as the non-symmorphic symmetry and orbital characters.

Spin-momentum-layer locking.—In addition to the momentum dependence and high spin polarization, there is another feature of the HSP at the X point, namely, the spin texture that is localized on the measured sector, manifesting a novel way of spin-momentum-layer locking [40–42]. As shown in Fig. 2 and Ref. [29], for the horizontal $M - X$ line and horizontal $\Gamma - X$ line, the S_y component is strong, while the S_x component vanishes. Similarly, for the vertical $\Gamma - X$ line, the S_x component is strong, while the S_y component vanishes. Since the S_z component is considerably less intense than the in-plane ones [29], this finding indicates a perpendicular spin orientation to the wave vector lying in the $k_x - k_y$ plane. We have further confirmed the specific spin texture for all the three pairs of valance bands, as illustrated in Figs. 3(a) and 3(b); note that only the spin textures of VB1, VB3, and VB5 are shown in Fig. 3(b), while the spin orientations of VB2, VB4, and VB6 are opposite to their counterparts. Surprisingly, while the VB1-2 pair shows a weak spin polarization, VB3-4 and VB5-6 pairs exhibit Dresselhaus-type spin textures with large magnitude, rather than the Rashba spin polarization induced by the local polar field.
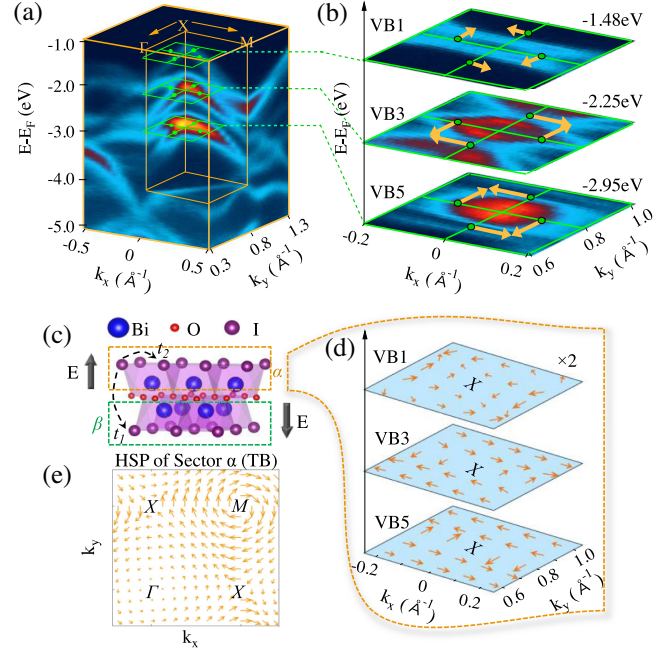

FIG. 3. (a) Overview of ARPES-measured spectra of BiOI plotted in the $k_x - k_y - E$ space. (b) Schematic sketch of the measured spin textures of VB1, VB3, and VB5 by spin ARPES, with the momentum cross sections denoted by the green squares in panel (a). (c) The layered structure of BiOI with two BiI sectors experiencing opposite local dipole fields (black arrows). (d) DFT calculation for p_z-projected HSP of VB1, VB3, and VB5 around X for the sector α. The spin magnitude of VB1 is multiplied by a factor of 2. (e) Spin texture for the sector α calculated by our tight-binding model, showing Dresselhaus and Rashba type HSP effects for X and M, respectively.

Here we employed the p-polarization geometry, where the vector potential of the incident photon lies on the incidence plane. Based on the dipole selection rule [43,44], the p_x and p_z orbitals are selectively detected. Furthermore, by changing the incidence angle of photons, one can change the ratio of the vector potential components parallel ($A_\parallel$) and perpendicular ($A_\perp$) to the sample surface. The dipole transition matrix element for the p_z (p_x) orbital is in proportion to the magnitude of the $A_\perp$ ($A_\parallel$) component, and $A_\perp$ is larger than $A_\parallel$ in the present geometry. In our orbital-projected band calculation in Fig. 1(c), the VB3-6 bands at the X point and the VB1-2 bands at the M point are mainly derived from the p_z orbital. Therefore, we have performed DFT calculations on the p_z-projected spin textures localized on the top BiI layer, i.e., sector α, as shown in Figs. 3(c) and 3(d). We found qualitative agreement with the counterparts measured by spin ARPES in Fig. 3(b). All three VB pairs exhibited weak spin polarization (<20%) around the Γ point [29]. As shown in Fig. 3(d), in the vicinity of X, only the VB1-2 pair manifested very weak spin polarization due to the tiny contribution of the p_z orbital of these bands [see Fig. 1(c)]. In comparison, the spin textures of VB3-4 and VB5-6 around X exhibited a

Dresselhaus type pattern with considerable magnitude. Moreover, the spin patterns of VB3 and VB5 are opposite to each other, which also agrees with the experiment. Thus, we have concluded that the DFT results successfully reproduce the features of the experimental observations, confirming the fact that the measured spin polarization originates from the intrinsic HSP in BiOI.

To further understand the mechanism of the momentum-dependent HSP effect and the corresponding spin-momentum locking, especially the Dresselhaus spin textures at the X point, we have constructed a single-orbital tight-binding model of a nonsymmorphic $P4/nmm$ structure. Two p_z orbitals of the iodine atoms on the adjacent sectors α and β, connected by the glide mirror operation $\{M_z|(\frac{1}{2}, \frac{1}{2}, 0)\}$, were chosen, as shown in Fig. 3(c). Under the basis of $\{|\alpha\uparrow\rangle, |\alpha\downarrow\rangle, |\beta\uparrow\rangle, |\beta\downarrow\rangle\}$, the model Hamiltonian can be written as [16]

$$H(k) = t_1 \cos\frac{k_x}{2}\cos\frac{k_y}{2}\tau_x \otimes \sigma_0 + t_2(\cos k_x + \cos k_y)\tau_0 \otimes \sigma_0$$
$$+ \lambda\tau_z \otimes (\sigma_y \sin k_x - \sigma_x \sin k_y). \tag{1}$$

Here, τ and σ are Pauli matrices under the basis of $\{|\alpha\rangle, |\beta\rangle\}$ and $\{|\uparrow\rangle, |\downarrow\rangle\}$, respectively; t_1 (t_2) is the intersector (intrasector) electron hopping that contributes to the Hamiltonian's diagonal (off-diagonal) terms. The third term of Eq. (1) describes the SOC effect induced by the local symmetry breaking for each sector, parametrized by λ. It is noticeable that at the boundary of the BZ, e.g., the $X - M$ line, Eq. (1) naturally becomes block diagonal for $\{|\alpha\uparrow\rangle, |\alpha\downarrow\rangle\}$ and $\{|\beta\uparrow\rangle, |\beta\downarrow\rangle\}$, having opposite local spin polarizations for each sector. When the probe sees sector α predominately, i.e., after breaking the symmetry between α and β, Eq. (1) is naturally decomposed into two matrices for each sector, and thus, the HSP of the sector α is measurable. In contrast, the HSP effect is substantially suppressed around the Γ point due to the intersector coupling t_1 term, as shown in Fig. 3(e), leading to the negligible spin signal measured from spin ARPES. We note that besides nonsymmorphic symmetry, the inclusion of multiple orbitals (such as three p orbitals) could lead to a different type of interference effect that modulates the momentum-dependent spin polarization [16,24].

Our tight-binding model also helps to understand the specific spin textures around different high-symmetry momenta. The low-energy effective $k \cdot p$ Hamiltonian derived from Eq. (1) has the form of $(k_x\sigma_y - k_y\sigma_x)\tau_z$ at M and $(k_x\sigma_y + k_y\sigma_x)\tau_z$ at X, indicating Rashba and Dresselhaus type HSP, respectively, and the latter perfectly explaining the measured spin polarization around the X point. Such results indicate that although a (local) polar field existing in a crystal in general supports a (hidden) Rashba-type spin polarization, a (hidden) Dresselhaus-type spin polarization would also be accompanied [11], depending on the specific symmetry of given momenta.

In summary, combining spin-ARPES measurements and theoretical calculations, we report distinct spin-momentum-layer locking phenomena at different BZ positions in a centrosymmetric material BiOI. The measured spin polarization localized on a specific BiI layer is highly polarized along the BZ boundary but almost vanishes around the zone center due to its nonsymmorphic crystal structure. The layer-resolved spin texture, either Rashba or Dresselhaus type, reflects the symmetry of both real space and k space. Our findings experimentally demonstrate the existence of the HSP effect and shed light on the design metrics to utilize high spin polarization in centrosymmetric materials by revealing the intimate interplay between spin, orbital, and layer degrees of freedom.

*These authors contributed equally to this work.
†kshimada@hiroshima-u.ac.jp
‡chency@sustech.edu.cn
§liuqh@sustech.edu.cn

[1] S. Datta and B. Das, Electronic analog of the electro-optic modulator, Appl. Phys. Lett. 56, 665 (1990).

[2] I. Žutić, J. Fabian, and S. D. Sarma, Spintronics: Fundamentals and applications, Rev. Mod. Phys. 76, 323 (2004).

[3] H. C. Koo, J. H. Kwon, J. Eom, J. Chang, S. H. Han, and M. Johnson, Control of spin precession in a spin-injected field effect transistor, Science 325, 1515 (2009).

[4] A. Manchon, H. C. Koo, J. Nitta, S. Frolov, and R. Duine, New perspectives for Rashba spin–orbit coupling, Nat. Mater. 14, 871 (2015).

[5] A. Soumyanarayanan, N. Reyren, A. Fert, and C. Panagopoulos, Emergent phenomena induced by spin–orbit coupling at surfaces and interfaces, Nature (London) 539, 509 (2016).

[6] X. Lin, W. Yang, K. L. Wang, and W. Zhao, Two-dimensional spintronics for low-power electronics, National electronics review **2,** 274 (2019).

[7] *Spin-Orbit Coupling in Two-Dimensional Electron and Hole Systems*, edited by R. Winkler, S. Papadakis, E. De Poortere, and M. Shayegan (Springer, New York, 2003).

[8] G. Dresselhaus, Spin-orbit coupling effects in zinc blende structures, Phys. Rev. **100,** 580 (1955).

[9] E. I. Rashba, Properties of semiconductors with an extremum loop. 1. Cyclotron and combinational resonance in a magnetic field perpendicular to the plane of the loop, Sov. Phys. Solid State **2,** 1109 (1960), https://www.elibrary.ru/item.asp?id=21757915.

[10] Q. Liu, Y. Guo, and A. J. Freeman, Tunable Rashba effect in two-dimensional $LaOBiS_2$ films: Ultrathin candidates for spin field effect transistors, Nano Lett. **13,** 5264 (2013).

[11] X. Zhang, Q. Liu, J.-W. Luo, A. J. Freeman, and A. Zunger, Hidden spin polarization in inversion-symmetric bulk crystals, Nat. Phys. **10,** 387 (2014).

[12] L. Yuan, Q. Liu, X. Zhang, J.-W. Luo, S.-S. Li, and A. Zunger, Uncovering and tailoring hidden Rashba spin–orbit splitting in centrosymmetric crystals, Nat. Commun. **10,** 906 (2019).

[13] Q. Liu, X. Zhang, and A. Zunger, Intrinsic Circular Polarization in Centrosymmetric Stacks of Transition-Metal Dichalcogenide Compounds, Phys. Rev. Lett. **114,** 087402 (2015).

[14] Q. Liu, X. Zhang, H. Jin, K. Lam, J. Im, A. J. Freeman, and A. Zunger, Search and design of nonmagnetic centrosymmetric layered crystals with large local spin polarization, Phys. Rev. B **91,** 235204 (2015).

[15] J. M. Riley, F. Mazzola, M. Dendzik, M. Michiardi, T. Takayama, L. Bawden, C. Granerød, M. Leandersson *et al.*, Direct observation of spin-polarized bulk bands in an inversion-symmetric semiconductor, Nat. Phys. **10,** 835 (2014).

[16] Y. Zhang, P. Liu, H. Sun, S. Zhao, H. Xu, and Q. Liu, Symmetry-assisted protection and compensation of hidden spin polarization in centrosymmetric systems, Chin. Phys. Lett. **37,** 087105 (2020).

[17] W. Yao, E. Wang, H. Huang, K. Deng, M. Yan, K. Zhang, K. Miyamoto, T. Okuda *et al.*, Direct observation of spin-layer locking by local Rashba effect in monolayer semiconducting $PtSe_2$ film, Nat. Commun. **8,** 14216 (2017).

[18] M. Gehlmann, I. Aguilera, G. Bihlmayer, E. Młyńczak, M. Eschbach, S. Döring, P. Gospodarič, S. Cramm *et al.*, Quasi 2D electronic states with high spin-polarization in centrosymmetric MoS_2 bulk crystals, Sci. Rep. **6,** 26197 (2016).

[19] K. Deng, M. Yan, C.-P. Yu, J. Li, X. Zhou, K. Zhang, Y. Zhao, K. Miyamoto *et al.*, Crossover from 2D metal to 3D Dirac semimetal in metallic $PtTe_2$ films with local Rashba effect, Sci. Bull. **64,** 1044 (2019).

[20] D. Santos-Cottin, M. Casula, G. Lantz, Y. Klein, L. Petaccia, P. Le Fèvre, F. Bertran, E. Papalazarou, M. Marsi, and A. Gauzzi, Rashba coupling amplification by a staggered crystal field, Nat. Commun. **7,** 11258 (2016).

[21] J. Tu, X. Chen, X. Ruan, Y. Zhao, H. Xu, Z. Chen, X. Zhang, X. Zhang *et al.*, Direct observation of hidden spin polarization in 2H-$MoTe_2$, Phys. Rev. B **101,** 035102 (2020).

[22] E. Razzoli, T. Jaouen, M.-L. Mottas, B. Hildebrand, G. Monney, A. Pisoni, S. Muff, M. Fanciulli *et al.*, Selective Probing of Hidden Spin-Polarized States in Inversion-Symmetric Bulk MoS_2, Phys. Rev. Lett. **118,** 086402 (2017).

[23] S.-L. Wu, K. Sumida, K. Miyamoto, K. Taguchi, T. Yoshikawa, A. Kimura, Y. Ueda, M. Arita *et al.*, Direct evidence of hidden local spin polarization in a centrosymmetric superconductor $LaO_{0.55}F_{0.45}BiS_2$, Nat. Commun. **8,** 1919 (2017).

[24] K. Gotlieb, C.-Y. Lin, M. Serbyn, W. Zhang, C. L. Smallwood, C. Jozwiak, H. Eisaki, Z. Hussain, A. Vishwanath, and A. Lanzara, Revealing hidden spin-momentum locking in a high-temperature cuprate superconductor, Science **362,** 1271 (2018).

[25] R. Suzuki, M. Sakano, Y. Zhang, R. Akashi, D. Morikawa, A. Harasawa, K. Yaji, K. Kuroda *et al.*, Valley-dependent spin polarization in bulk MoS_2 with broken inversion symmetry, Nat. Nanotechnol. **9,** 611 (2014).

[26] R. Oliva, T. Woźniak, F. Dybala, J. Kopaczek, P. Scharoch, and R. Kudrawiec, Hidden spin-polarized bands in semiconducting 2H-$MoTe_2$, Mater. Res. Lett. **8,** 75 (2020).

[27] Y. Huang, A. Yartsev, S. Guan, L. Zhu, Q. Zhao, Z. Yao, C. He, L. Zhang *et al.*, Hidden spin polarization in the centrosymmetric MoS_2 crystal revealed via elliptically polarized terahertz emission, Phys. Rev. B **102,** 085205 (2020).

[28] M. Arumugam and M. Y. Choi, Recent progress on bismuth oxyiodide (BiOI) photocatalyst for environmental remediation, J. Ind. Eng. Chem. **81,** 237 (2020).

[29] See Supplemental Material at http://link.aps.org/supplemental/10.1103/PhysRevLett.127.126402 for theoretical and experimental methods, DFT calculated bands of BiOI, sample characterization, photon energy dependent ARPES results, spin polarizations along vertical and horizontal $\Gamma - X$ lines, spin components along the $\Gamma - X$ and $M - X$ directions, out-of-plane spin polarization, and spin textures of six valance bands in the first BZ, which includes Refs. [11,16,28,30–36].

[30] *Very High Resolution Photoelectron Spectroscopy*, edited by S. Hüfner (Springer, New York, 2007).

[31] H. Iwasawa, K. Shimada, E. Schwier, M. Zheng, Y. Kojima, H. Hayashi, J. Jiang, M. Higashiguchi *et al.*, Rotatable high-resolution ARPES system for tunable linear-polarization geometry, J. Synchrotron Radiat. **24,** 836 (2017).

[32] T. Okuda, K. Miyamaoto, H. Miyahara, K. Kuroda, A. Kimura, H. Namatame, and M. Taniguchi, Efficient spin resolved spectroscopy observation machine at Hiroshima Synchrotron Radiation Center, Rev. Sci. Instrum. **82,** 103302 (2011).

[33] G. Kresse and D. Joubert, From ultrasoft pseudopotentials to the projector augmented-wave method, Phys. Rev. B **54,** 11169 (1996).

[34] P. Hohenberg and W. Kohn, Inhomogeneous electron gas, Phys. Rev. B **136,** B864 (1964).

[35] W. Kohn and L. J. Sham, Self-consistent equations including exchange and correlation effects, Phys. Rev. **140,** A1133 (1965).

[36] G. Kresse and D. Joubert, From ultrasoft pseudopotentials to the projector augmented-wave method, Phys. Rev. B **59,** 1758 (1999).

[37] We note that a trade-off between the measurement efficiency and energy resolution in the spin-ARPES measurement must be considered. We have chosen the current resolution configuration to experiment within a reasonable time, consequently sacrificing the ability to resolve all the individual VB peaks in spin-resolved EDCs.

[38] C. J. Powell, A. Jablonski, I. Tilinin, S. Tanuma, and D. R. Penn, Surface sensitivity of Auger-electron spectroscopy and X-ray photoelectron spectroscopy, J. Electron Spectrosc. Relat. Phenom. **98–99**, 1 (1999).

[39] C. Yu, C. Fan, C. Y. Jimmy, W. Zhou, and K. Yang, Preparation of bismuth oxyiodides and oxides and their photooxidation characteristic under visible/UV light irradiation, Mater. Res. Bull. **46**, 140 (2011).

[40] A. M. Jones, H. Yu, J. S. Ross, P. Klement, N. J. Ghimire, J. Yan, D. G. Mandrus, W. Yao, and X. Xu, Spin-layer locking effects in optical orientation of exciton spin in bilayer WSe_2, Nat. Phys. **10**, 130 (2014).

[41] X. Xu, W. Yao, D. Xiao, and T. F. Heinz, Spin and pseudospins in layered transition metal dichalcogenides, Nat. Phys. **10**, 343 (2014).

[42] X. Xi, Z. Wang, W. Zhao, J.-H. Park, K. T. Law, H. Berger, L. Forró, J. Shan, and K. F. Mak, Ising pairing in superconducting $NbSe_2$ atomic layers, Nat. Phys. **12**, 139 (2016).

[43] A. Damascelli, Z. Hussain, and Z.-X. Shen, Angle-resolved photoemission studies of the cuprate superconductors, Rev. Mod. Phys. **75**, 473 (2003).

[44] Y. Cao, J. Waugh, X. Zhang, J.-W. Luo, Q. Wang, T. Reber, S. Mo, Z. Xu *et al.*, Mapping the orbital wavefunction of the surface states in three-dimensional topological insulators, Nat. Phys. **9**, 499 (2013).